Volcanoes get warm for years prior to eruption

Társilo Girona[1], Vincent Realmuto[1], and Paul Lundgren[1]

[1]Jet Propulsion Laboratory, California Institute of Technology, Pasadena, CA 91109, USA.

Identifying the observables that warn of volcanic eruptions is a major challenge in natural disasters management. An important, but under-investigated, observable is the diffuse heating of volcanic soils, which represents a major energy source at quiescent volcanism. However, it remains unclear whether diffuse heating, or surface warming, responds to pre-eruptive processes and varies before eruption. Here we show that the last eruptions/explosions of seven different volcanoes were preceded by a systematic long-term (~years) warming of their flanks. This warming, found through a new statistical analysis of satellite-based long-wavelength (10.780–11.280 μm) infrared data, is a phenomenon that operates over large areas (from a few to hundreds of km^2) of the volcanic edifices. Specifically, the median temperature of the target volcanoes increased with respect to the surroundings by up to ~1.5 ℃ for several years before magmatic, phreatic, and hydrothermal eruptions. This reflects heat flux increases of up to ~10 W/m^2, probably driven by the enhancement of subsurface hydrothermal activity. Surface warming is detected even before eruptions that were impossible to anticipate through other geophysical/geochemical methods (e.g., the 2014 phreatic eruption of Ontake, Japan; the 2015 magmatic eruption of Calbuco, Chile), thus opening new horizons to better constrain the thermal budget of volcanoes and improve eruption forecasts.

Volcanoes are major emitters of the Earth's internal heat. A large amount of heat is released diffusively through the soil[1–5] (e.g., ~0.9 MW at Masaya, Nicaragua; ~3.6 MW at Pantelleria, Italy; ~16.6 MW at Vesuvio, Italy; ~42.6 MW at Nisyros, Greece; ~100.8 MW at Campi Flegrei, Italy), which represents the dominant energy source during inter-eruptive periods. For example, *Chiodini et al.*[6] found that diffuse heating at the Solfatara crater dominates the energy budget of Campi Flegrei caldera, and that is one order of magnitude greater than the elastic energy released during recent seismic and deformation episodes. *Mannini et al.*[7] also reported that diffuse heating accounts for >90% of the total heat flux of Vulcano's Fossa fumarole field (Italy). These studies stimulate the following questions: Does diffuse heating operate over large areas of volcanic edifices or is it only constrained to fumarolic fields? Is there a link between diffuse heating and the subsurface processes that drive eruptions? To what extent does diffuse heating vary before eruptions?

Surface warming detection algorithm and case studies

This work addresses the aforementioned questions by analyzing 16.5-year records (between 04-July-2002 and 31-January-2019) of the thermal infrared radiance measured by the Moderate Resolution Imaging Spectroradiometers (MODIS) aboard NASA's Terra and Aqua satellites. In particular, we examined day- and night-time scenes from MODIS Band 31 (10.780-11.280 μm), which captures surface radiance variations with minimal effects from atmospheric absorption and emission[8]. MODIS is well suited for our study because it provides global coverage with high temporal resolution (~2 observations per day at tropical latitudes); wide ground swaths with simultaneous information of large areas (~2,330 km at tropical latitudes); and spatial resolution of

~1 km^2 at nadir, sufficient to detect diffuse heating as long as it occurs over extensive areas. Ground-based measurements of soil temperature provide higher accuracy, but they are only available at a few volcanoes and are obtained over short time periods and/or over small areas (typically <1 km^2) of the volcanic flanks[9–14].

Space-based thermal remote sensing of volcanoes has been performed using metrics detecting hotspots[15–21], i.e., small-scale (~pixel size) locations that are hotter than their surroundings due to magma or fumarolic activity. In contrast, we aim to investigate large-scale (~volcanic edifice size) heat emissions (Fig. 1), which requires designing a statistical metric that tracks the thermal energy escaping from the volcanic flanks and that minimizes the effects of "outliers" in the data records due to cloud coverage, geolocation errors, pixel mosaicking, or overlap between scan lines[8]. These requirements are met by the median anomaly ($\overline{\delta T}$), a new metric that captures the long-term (~years) variation of the lowest temperature of a volcanic edifice with respect to its surroundings (see Methods and Supplementary Methods).

This study focuses on exploring the temporal evolution of $\overline{\delta T}$ for seven volcanoes that are representative of many volcanoes around the world, cover a broad range of behaviors and characteristics, and have erupted/exploded over the past two decades (Ontake, Japan; Ruapehu, New Zealand; Domuyo, Argentina; Calbuco, Chile; Redoubt, Alaska; Agung, Indonesia; and Pico do Fogo, Cape Verde). In particular, these volcanic systems cover different: (a) eruption type (hydrothermal, phreatic, or magmatic) and magnitude (Volcanic Explosivity Index or VEI=0-4); (b) evolution; (c) degree of hydrothermal activity at the surface; (d) levels of pre-eruptive unrest

and post-eruptive behavior; (e) ground covers (permanent glaciers or snow, seasonal snow, crater lake, arid areas, forest and rainforest); (f) latitude (from ~8° to ~60°); and (g) origin (i.e., formed over crustal plate boundaries or forming islands over hotspots). The only requirement imposed in the choice of the volcanoes is that our statistical algorithm must be applicable. This implies that the volcanoes: (i) must have erupted only once or twice over the last two decades because our algorithm does not capture thermal processes occurring in short (<1 year) timescales; (ii) must not be located in very small islands because our algorithm requires sufficient number of pixels for the statistical analysis to be robust; (iii) must be significantly elevated with respect to the surroundings, so our algorithm can successfully identify scenes little affected by clouds.

Pre-eruptive surface warming of volcanic flanks

Our analysis reveals that the eruptions/explosions of our test cases occurred around the highest values of the median anomaly $\overline{\delta T}$, and that they were preceded by a subtle but significant long-term (>1 year) warming ($\sim 0.1 - 1.5$ ℃) whose uncertainty is smaller (<40%) for large events (Fig. 2; Table 1). In addition, $\overline{\delta T}$ decreases right after small eruptions (VEI<3, or a few months after eruptions if they are large (VEI≥ 3). Right after large eruptions, $\overline{\delta T}$ increases quickly due to the materials deposited around the vent, which modify surface temperature and emissivity. Below, we describe the results obtained for each volcano.

Ontake featured two unexpected events, a small (VEI=0) gas explosion in March 2007 and a large (VEI=3) phreatic eruption in September 2014 (which killed around 60 hikers[22] and became the worst volcanic disaster in Japan since 1926) (Fig. 2a). The median anomaly $\overline{\delta T}$ increased by ~0.20 ℃ between January 2004 and March 2007, when the small gas explosion occurred. After

this explosion, $\overline{\delta T}$ decreased gradually at an average rate of ~ 0.14 ℃/year, until reaching the minimum value of the time series in mid-2012. Then, $\overline{\delta T}$ increased by 0.72 ± 0.21 ℃ for about two years (the fastest pre-eruptive warming of the test cases, together with Agung), reaching $\overline{\delta T} = 0.85 \pm 0.15$ ℃ by the time of the large 2014 phreatic eruption[22]. The ~2-year precursory warming of the 2014 eruption is apparently linked neither to long-term seismic and geodetic observations around the volcano[22] nor to helium anomalies[23]. No other well-defined long-term warning sign has been detected so far for the 2014 eruption.

Ruapehu featured two unheralded events, a small (VEI=1) gas explosion in October 2006 and a larger phreatomagmatic eruption (VEI=1) in September 2007 (in which a climber suffered serious injuries[24]) (Fig. 2b). The median anomaly $\overline{\delta T}$ increased by 0.65 ± 0.23 ℃ during, at least, the 3-to-4 years preceding the 2006 explosion and the 2007 eruption. This pre-eruptive warming coincides with the enhancement of seismic attenuation[25], and partially with the tidal modulation of the shallow seismicity[26]. Since the 2007 eruption, the thermal anomaly has remained at high levels ($\overline{\delta T} \sim 0.6 - 0.8$ ℃) compared to 2004 ($\overline{\delta T} \sim 0.2 - 0.3$ ℃), concomitant with several unrest episodes. It is worth highlighting a decrease of $\overline{\delta T}$ from the end of 2011 to mid-2015, coinciding in part with a sustained period of low lake temperatures (from mid-2012 to mid-2013); and a small upturn of ~0.15 ℃ between 2014-2017, coinciding with strong tremor levels, anomalous earthquakes, and high degassing rates and lake temperatures[26].

Domuyo has not presented major Holocene eruptions, although it is the second most energetic hydrothermal system on Earth (after Yellowstone) and minor unheralded hydrothermal explosions in February 2003, January 2007, and August 2012 were reported by local people and park

rangers[27,28] (Fig. 2c). The 2003 hydrothermal explosion occurred at the edge of the $\overline{\delta T}$ time series, so the pre-eruptive variation of the median anomaly cannot be assessed for that event. The 2007 and 2012 events were preceded by $\overline{\delta T}$ increases in the range 0.15-0.95 ℃ since 2004 and up to ~0.50 ℃ since 2009, respectively. The uncertainty band is wider at this volcano, although the minor explosions occurred at the highest levels of the median anomaly (0.93 ± 0.41 ℃ and 0.86 ± 0.42 ℃, respectively). From 2012 to late 2016, the median anomaly decreased at average rates of ~0.25 ℃/year. Since then, $\overline{\delta T}$ has been increasing quickly at rates similar to those observed prior to the 2007 explosion.

Calbuco featured a large but unheralded magmatic eruption[29] (VEI=4) in April-May 2015 (Fig. 2d). The median anomaly rose slowly by 0.32 ± 0.13 ℃ between 2008 and 2012; then, it remained roughly constant until the onset of the 2015 magmatic eruption. After the eruption, $\overline{\delta T}$ increased at much larger rates until reaching $\overline{\delta T}$~0.52 ℃ by the end of 2015; and since 2017, $\overline{\delta T}$ has been decreasing quickly. The pre-eruptive increase of $\overline{\delta T}$ suggests that the quick (<4 days) ascent of magma[29,30] expelled during the 2015 event was indeed preceded by a much long-term build-up process (e.g., slow accumulation of magma or gases in the shallow crust) that initiated about seven years earlier leaving a detectable thermal signature at the surface. A subtle long-term slow build-up to eruption may explain why no deformation was detected prior to the 2015 eruption[29].

Redoubt had a prominent (VEI=3) magmatic eruption[31] in March 2009 (Fig. 2e). The median anomaly increased by 0.47 ± 0.17 ℃ from mid-2006 to the 2009 magmatic eruption (~0.17 ℃/year on average); about one year after the event, $\overline{\delta T}$ started to decrease at accelerated rates for about five years. Since 2014, $\overline{\delta T}$ has remained at low levels ($\lesssim 0.3$ ℃), slightly above the values

found years before the 2009 eruption. Interestingly, $\overline{\delta T}$ began to increase ~1 year earlier than other precursory signals[31] (e.g., sulfur odors, increased gas emissions, deep seismicity, deformation, glacier melting).

Agung featured a large magmatic eruptive phase (VEI=3) between November 2017 and June 2019 (Fig. 2f). The median anomaly $\overline{\delta T}$ rose by 1.42 ± 0.27 ℃ between 2013 and the onset of the eruption in 2017 (~ 0.35 ℃/year on average), thus revealing that thermal unrest initiated several years before other pre-eruptive signals were detected (e.g., seismic activity increased ~3 months before the eruption[32]). The eruption occurred at the edge of the $\overline{\delta T}$ time series, and thus the post-eruptive evolution of the median anomaly cannot be assessed in this case. Interestingly, $\overline{\delta T}$ values around 2003-2004 are comparable to those prior to the 2017-2019 event, although the previous documented eruption occurred more than 50 years ago. This may reflect a previously undetected eruption at the beginning of the century, a failed eruption, or other processes such as large fires in the volcanic flanks. In fact, large fires were proposed to be responsible for several hotspots detected from space[33] in 2001 and 2002.

Pico do Fogo is a hotspot volcano that erupted magma (VEI=3) between November 2014 and February 2015 (Fig. 2g), and has been found to release diffuse magmatic CO_2 over extensive areas[34,35]. The onset of this eruption, which displaced more than 1,000 people and destroyed hundreds of buildings and hectares of agricultural land[36], was preceded by an increase of the median anomaly of 0.82 ± 0.23 ℃ since mid-2010 (~ 0.20 ℃/year on average). Similar to other volcanoes, $\overline{\delta T}$ increased quickly after the eruption and decreased a few months afterwards; in addition, thermal unrest initiated much earlier than other warning signs were detected (e.g.,

160 increasing diffuse CO_2 was detected only a few months before the event[36]). Interestingly, our
161 analysis also reveals a less prominent but significant thermal unrest between 2004 and 2008.
162 However, there is limited information between the 1995 and the 2014-2015 eruptions to assess
163 whether this thermal unrest was concomitant to other geophysical/geochemical warning signs or
164 whether it culminated in some kind of undetected activity at the surface.
165
166 **Heat flux and enhancement of hydrothermal activity**
167 Below, we discuss four possible explanations for the pre-eruptive surface warming detected in the
168 target volcanoes. First, the variations of the median anomaly ($\overline{\delta T}$) are spurious signals produced
169 by noise (see Methods). This is not realistic because the probability of obtaining the observed
170 amplitudes of $\overline{\delta T}$ by chance is 3.3% at most (for Domuyo), and is below 0.01% for Ontake and
171 Redoubt (Fig. 2f). This means that our results represent actual thermal variations beyond the 2-
172 sigma confidence level, reaching much higher confidence levels for most of the volcanoes. Second,
173 the pre-eruptive variations of $\overline{\delta T}$ are dominated by atmospheric/weather phenomena, the stability
174 of the MODIS sensors, and/or fires. Although these processes may play a significant role (e.g.,
175 fires may be responsible for the high thermal emissions detected at Agung volcano at the beginning
176 of the XXI century[33]), the systematic increase of $\overline{\delta T}$ prior to eruption or during volcanic unrest
177 suggest that it is dominated by subsurface volcanic processes. Third, the pre-eruptive variations of
178 $\overline{\delta T}$ reflect the emergence of volcano-related hotspots (i.e., lava domes or fumaroles). This is not
179 feasible because gradual long-term median temperature variations reflect gradual shifts of the
180 temperature distribution of the volcanic flanks. The emergence of volcano-related hotspots can
181 produce step variations of the median of the temperature distribution but not gradual long-term
182 changes, unless they emerge gradually over the large areas explored, which is not realistic. Fourth,

the pre-eruptive thermal variations observed in the target volcanoes reflect the diffuse supply of heat to the surface, which slightly warms up the soil and snow cover[37] over extensive (~edifice size) areas (Fig. 1). Diffuse heating is the only physically realistic explanation for our results.

We theorize that the large-scale surface warming of volcanoes reflects the enhancement of subsurface hydrothermal activity (Fig. 1). In particular, the gas exsolved in shallow magma reservoirs rises via permeable flow through the crust, and dissipates heat through interaction with the host rock and through boiling in underground aquifers[6]. The water vapor from boiling aquifers and from magma (mixed with other magmatic gases, e.g., CO_2) rises towards the surface, and eventually condenses beneath the soil when the proper thermodynamic conditions are reached[9]. The condensation of H_2O releases latent heat that is then transported to the surface through conductive heat transfer in the uppermost part of the soil[1,6,10]. The pre-eruptive variation of heat flux supplied to the surface between two instants t and t_0, $\Delta\Phi_d(t;t_0)$, can be estimated from a heat balance model using the median anomaly (Supplementary Methods):

$$\Delta\Phi_d(t;t_0) \approx 4\sigma\varepsilon T^3\left[\overline{\delta T}(t) - \overline{\delta T}(t_0)\right] \quad , \qquad (1)$$

where $\sigma = 5.67 \cdot 10^{-8}\ \mathrm{W/m^2K^4}$ is the Stefan-Boltzmann constant; ε is the time-averaged median surface emissivity of the area analyzed (and for the central wavelength of the band used in this study; ~11 μm); and T is the time-averaged median brightness temperature of the regional background. For example, for the unheralded 2014 Ontake ($T = 274 \pm 24$ ℃, $\overline{\delta T}(t) - \overline{\delta T}(t_0) = 0.72 \pm 0.21$ ℃, $\varepsilon = 0.95 \pm 0.05$) and 2015 Calbuco ($T = 278 \pm 18$ ℃, $\overline{\delta T}(t) - \overline{\delta T}(t_0) =$

0.32 ± 0.13 ℃, $\varepsilon = 0.95 \pm 0.05$) eruptions, we obtain pre-eruptive increases of heat flux of $\Delta\Phi_d(t; t_0) = 3.2 \pm 1.3$ W/m^2 and $\Delta\Phi_d(t; t_0) = 1.50 \pm 0.69$ W/m^2, respectively, whereas it reaches values of $\Delta\Phi_d(t; t_0) = 7.42 \pm 2.37$ W/m^2 for Agung ($T = 289 \pm 24$ ℃, $\overline{\delta T}(t) - \overline{\delta T}(t_0) = 1.42 \pm 0.27$ ℃, $\varepsilon = 0.95 \pm 0.05$) (Table 1; Supplementary Table 1). Interestingly, the pre-eruptive increase of heat flux appears to be independent of the type of eruption (i.e., gas-dominated eruptions or magma-dominated); this supports the idea that large-scale diffuse heating reflects the ascent of magmatic gas to the surface and its interaction with hydrothermal systems.

This work demonstrates that diffuse heating is a large-scale phenomenon operating over extensive areas of volcanic edifices (similar to diffuse degassing[34,38,39]), is an early indicator of volcanic reactivation, increases prior to different types of eruption, and can be tracked with a simple satellite-based remote sensing method. These findings open new horizons to explore the thermal budget of volcanoes and better forecast eruptions that are very difficult to anticipate through other geophysical methods (e.g., gas-driven events). Diffuse heating is probably controlled by the increasing supply of hot gases to the shallow crust, which enhances underground hydrothermal activity[40], subsoil steam condensation, and the transport of heat towards the surface[1,9]. In turn, the supply of gases from depth may be controlled by the ascent of magma to the surface, magma reservoir dynamics, and crust permeability[25,26]. Future work will pay special attention to the thermal evolution of Domuyo (Argentina), which shows ongoing warming; will apply our method to other sub-aerial volcanoes around the world; will explore the limitations to track diffuse heating in frequently-erupting volcanoes (e.g., Etna, Italy); and will focus on understanding the link between large-scale diffuse heating, heat emissions in fumarolic fields (i.e., hotspots), soil and plume degassing, and ground deformation.

METHODS

1) Data retrieval

Data from 04-July-2002 to 31-January-2019 are retrieved from the MODIS instruments aboard the Terra and Aqua satellites, launched in December 1999 and May 2002, respectively. MODIS products are a major component of the NASA's Earth Observing System, and their strengths include global coverage, high sampling rate (from ~1 to ~4 swaths per day per satellite, depending on latitude), high radiometric resolution, suitable dynamic range, and accurate calibration[8]. In particular, we investigate the thermal evolution of volcanic surfaces by using two products (https://earthdata.nasa.gov/): MODIS Terra/Aqua Calibrated Radiances 5-Min Level-1B Swath 1km V006 (MOD021KM/MYD021KM) and MODIS Terra/Aqua Geolocation Fields 5-Min Level-1A Swath 1km V006 (MOD03/MYD03). The Level-1B Radiance product provides accurate values of radiance, which have little or no long-term drift[41], are radiometrically calibrated, and are corrected for instrumental effects; the Level-1A Geolocation product provides the geographical coordinates of each pixel of the Level-1B scenes. Altogether, we analyze >200,000 MODIS scenes (26,277 for Ontake; 28,539 for Ruapehu; 27,429 for Domuyo; 30,338 for Calbuco; 46,896 for Redoubt; 21,242 for Agung; and 22,004 for Pico do Fogo), which correspond to >30 TB of memory. MODIS acquires radiance at spatial resolution of $\sim 1\ km^2$ at nadir in 16 thermal bands of the electromagnetic spectrum, but this study focuses only on band 31 (10.780-11.280 μm) because is more sensitive to surface temperature variations[8]. Note that we do not explore the thermal evolution of the ground with Land Surface Temperature (LST) products[42] because we want to use data with little previous processing.

2) Data Analysis

We implement a new statistical strategy to capture the long-term (~years) brightness temperature evolution of the coldest areas (~ 20 km^2 on average) of volcanic flanks; this is used as a proxy for the radiant changes in the volcanic edifices as a whole. This approach contrasts with previous algorithms aiming to detect the emergence of hotspots[15–20] (i.e., pixels that are hotter than the surrounding pixels) associated with magma exposure at the surface or fumarolic activity. Our algorithm consists of six main steps (Supplementary Fig. 1).

2.1) Choice of exploration areas

We choose latitude-longitude quadrangles (0.30° latitude by 0.48° longitude) centered at the geographical coordinates of the volcanoes under study (as provided by the Smithsonian Institution's Global Volcanism Program database; https://volcano.si.edu/). These quadrangles cover the volcanic edifices and their surroundings, and represent surface areas A_t on the order of $\sim 900 - 1{,}500$ km^2 and number of pixels at nadir in the range $N \approx 900 - 1{,}500$, depending on the latitude of the volcanoes (Supplementary Fig. 1a, 1b). In addition, we choose an auxiliary subarea $A_{aux} < A_t$ covering part of the volcanic edifices only, and that ranges from ~50 km^2 to ~800 km^2 depending on topography (Supplementary Table 1). The auxiliary subarea is used only to automatically detect useless scenes and discard them.

2.2) Automatic discarding of useless scenes

We calculate different statistical estimators in the target areas A_t using the MODIS scenes. These estimators are the median spectral radiance of the M pixels with lowest spectral radiance ($L_{c,M}$)

and the median spectral radiance of the K pixels with largest spectral radiance ($L_{h,K}$). The median is chosen as the statistical estimator because it minimizes the outlier effects (e.g., due to cloud coverage, pixel mosaicking, geolocation errors, and overlap of scan lines[8]). In cloud-free scenes, the M pixels with lowest spectral radiance and the pixel with median spectral radiance $L_{c,M}$ fall into the subarea A_{aux} (Supplementary Fig. 1c), whereas the K pixels with largest spectral radiance and the pixel with median spectral radiance $L_{h,K}$ fall outside the subarea A_{aux} (Fig. 1d). This is so because the highest levels of the volcanoes are colder (and thus emit less radiance) due to altitude. $L_{c,M}$ is therefore a good estimator of the median spectral radiance of the coldest areas of the volcanic flanks, whereas $L_{h,K}$ is a good estimator of the median spectral radiance of the regional background. In contrast, in scenes that are very contaminated by clouds, the pixel with median spectral radiance $L_{c,M}$ does not fall into the subarea A_{aux} and/or the pixel with median spectral radiance $L_{h,K}$ falls into the subarea A_{aux}; when this happens, the scene is discarded (Supplementary Fig. 1e). It is worth noting that our algorithm always performs the same analysis, and thus our criterion allows us to discard scenes with high levels of cloudiness, but also scenes captured during post-eruptive periods (if hot magmatic products cover large areas of the volcanic flanks) and during days with temperature inversion (i.e., if the mountain is warmer than the surroundings due to atmospheric conditions). Our approach therefore allows us to automatically identify useless scenes, discard them, and thus maximally reduce the level of noise.

In particular, we use $M = 11$ pixels ($\sim 18 - 22$ km^2, on average, for the target volcanoes), $K = N - 101$ pixels (with N the total number of pixels within the target area A_t), and a subarea A_{aux} depending on the topography of each volcano (Supplementary Table 1). This yields a percentage of scenes discarded between ~29% for Domuyo and ~84% for Calbuco. In the worst-case scenario

(Calbuco), this implies 4,956 useful scenes for the 16.5-year period analyzed and thus 300 useful scenes per year on average. The use of slightly different values for M $(= 21, 31)$, K $(= N - 51, N - 201)$, and A_{aux} $(\pm 10\%)$ do not alter our overall results (Supplementary Fig. 2).

2.3) Contrast between coldest areas and regional background

For the scenes that are not discarded, we convert the statistical estimators $L_{c,M}$ and $L_{h,K}$ to brightness temperature for simplicity ($T_{c,M}$ and $T_{h,K}$, respectively) using the Planck's function:

$$T_x = \frac{C_2}{\lambda \, ln\left(1 + \frac{C_1}{\lambda^5 L_x}\right)} \quad , \quad (M1)$$

where L_x represents $L_{c,M}$ or $L_{h,K}$; T_x represents the brightness temperatures $T_{c,M}$ or $T_{h,K}$; $C_1 = 1.19 \cdot 10^{-16}$ m^2 W; $C_2 = 1.44 \cdot 10^{-2}$ m K; and λ is the central wavelength of band 31 (11.03 μm). Then, we calculate the difference $\Delta T_{M,K} = T_{c,M} - T_{h,K}$ (Supplementary Fig. 1f). This pursues the following goals: (a) to highlight any variation of brightness temperature occurring in the coldest parts of the volcanic flanks and not occurring in the area surrounding the volcano; (b) to minimize any local/regional atmospheric effect, as well as the possible artifacts of jointly combining daytime/nighttime scenes; and (c) to minimize the possible artifacts associated with the use of different sensors (MODIS/Terra and MODIS/Aqua).

2.4) Daily median brightness temperature difference

We compute the daily median brightness temperature difference ($\overline{\Delta T}_{M,K}(t)$, where t is time), i.e., the daily median of the statistical estimator $\Delta T_{M,K}$ (Supplementary Fig. 1g). This approach pursues

the following goals: (a) to produce a regular and continuous sampling rate (i.e., 1 sample/day), which facilitates signal processing; and (b) to minimize possible outliers associated with daytime/nighttime scenes. We use daytime and nighttime scenes to increase the sample population, and thus yield a more reliable statistical analysis (although the patterns obtained are essentially the same when using only daytime or nighttime scenes; see Supplementary Figure 3). The resulting time series ($\overline{\Delta T}_{M,K}(t)$) contains a seasonal component, noise, and gaps (produced by the discarding of useless scenes; section 2.2) that are filled through linear interpolation. In the worst-case scenario (Calbuco), we find 55% gaps in $\overline{\Delta T}_{M,K}(t)$, with the largest gap of 20 days, and 165 days per year (on average) with useful data (Supplementary Table S1). Although the large number of daily gaps hinders the detection of short-term (~days) anomalies, the number of valid scenes per year is suitable to detect long-term (~years) trends.

2.5) Low-pass filtering

After interpolation, the time series $\overline{\Delta T}_{M,K}(t)$ contains a well-defined seasonal component and noise; our aim is to bring out whether $\overline{\Delta T}_{M,K}(t)$ also contains hidden long-term (~years) trends (Supplementary Fig. 1h). To this outcome, we have designed an efficient low-pass filtering technique through >100,000 Monte Carlo experiments with synthetic time series $\overline{\Delta T}_{SYN}(t)$. The details of our numerical experiments are provided below:

1. We generate synthetic time series ($\overline{\Delta T}_{SYN}(t)$) combining a long-term trend ($\Delta T_{SYN}^{trend}(t)$), a seasonal component ($A_s sin\left(\frac{2\pi t}{365}\right)$), and a zero-mean Gaussian noise ($\Re(0, \sigma_d)$) with standard deviation σ_d:

$$\overline{\Delta T}_{SYN}(t) = \Delta T_{SYN}^{trend}(t) + A_s sin\left(\frac{2\pi t}{365}\right) + \Re(0, \sigma_d) \quad . \quad (M2)$$

We use $A_s = \sigma_d = 100$ and $\Delta T_{SYN}^{trend}(t) = \alpha_{imp} cos\big(2\pi(t - \tau_{imp})/T_{imp}\big)$, where α_{imp}, T_{imp}, and τ_{imp} are an imposed amplitude, period, and time lag, respectively (Supplementary Fig. 4a-4d).

2. For a given combination of α_{imp}, T_{imp}, and τ_{imp}, we filter the resulting time series $\overline{\Delta T}_{SYN}(t)$ through 480 different low-pass filtering methods (i.e., 24 filtering techniques that are applied iteratively up to $k = 20$ times; Supplementary Table 2) aiming to retrieve the imposed trend $\Delta T_{SYN}^{trend}(t)$. Iterative filtering methods are commonly used to improve the performance of noise reduction techniques[43]. The filtering methods explored include a combination of trailing moving mean, trailing moving median, MODWT (maximal overlap discrete wavelet transform), DWT (discrete wavelet transform), and Savitzky-Golay filters. The goodness of every denoising technique is assessed by computing the sinusoidal curve that best fits the filtered time series (with the non-linear least squares method), and then by calculating the coefficient of determination R^2, amplitude α_{ret}, period T_{ret}, and time lag τ_{ret} of the best fit curve. The values of R^2, α_{ret}, T_{ret}, and τ_{ret} are retrieved for 100 computer-generated synthetic time series $\overline{\Delta T}_{SYN}(t)$ with the same imposed values of α_{imp}, T_{imp}, and τ_{imp}, which are then used to calculate the mean coefficient of determination ($\overline{R^2}$), mean retrieved amplitude ($\bar{\alpha}_{ret}$), mean retrieved period ($\bar{T}_{ret}$), mean retrieved time lag ($\bar{\tau}_{ret}$), and their uncertainties (standard deviation). Finally, the values of $\overline{R^2}$, $\bar{\alpha}_{ret}$, $\bar{T}_{ret}$, $\bar{\tau}_{ret}$, and their uncertainties are calculated for different combinations of imposed amplitude, period, and time lag in the range $\alpha_{imp} = 2 - 90$, $T_{imp} = 5 - 20$ years, $\tau_{imp} = 0$. Under this

configuration, the signal-to-noise ratio (SNR; defined here as the variance of $\Delta T_{SYN}^{trend}(t)$ over the variance of $\overline{\Delta T}_{SYN}(t)$) varies in the range $SNR \approx 10^{-4} - 0.2$.

3. We assess which of the 480 low-pass filtering methods are the most appropriate to retrieve the imposed long-term (~years) trends (i.e., $\Delta T_{SYN}^{trend}(t)$) from the time series $\overline{\Delta T}_{SYN}(t)$. Our numerical experiments reveal that one of the most suitable methods is Technique 11 with $k = 10$ iterations (Supplementary Table 2), i.e., the combination of 10 MODWT filters (at level 10 and using symlets-8 wavelets, Donoho and Johnstone's universal soft thresholding, and level-dependent estimation of the noise) + 1 trailing moving median filter (of order 2 years) (Supplementary Fig. 5–8). For a vast combination of α_{imp} and T_{imp}, this method provides the highest values of the coefficient of determination, produces mean retrieved amplitudes ($\bar{\alpha}_{ret}$) and periods ($\bar{T}_{ret}$) that are compatible with the imposed values, and generates a mean time lag ($\bar{\tau}_{ret}$) on the order of ~1 year in the filtered signal that can be easily corrected. The filtering process, however, has several limitations that need to be taken into account: (a) if the signal-to-noise ratio is too low, our filtering process is not able to accurately retrieve hidden long-term trends from the $\overline{\Delta T}_{SYN}(t)$ time series. For example, for $T_{imp} = 15$ years, it is met that $\overline{R^2} \gtrsim 0.85$, $\bar{T}_{ret} \approx T_{imp}$, $\bar{\alpha}_{ret} \approx \alpha_{imp}$, and $\bar{\tau}_{ret} \approx 1\,\text{year}$ when $SNR \gtrsim 0.001$ only (Supplementary Fig. 9a-9d). (b) For decreasing values of the imposed periods T_{imp}, our method yields $\bar{\alpha}_{ret} < \alpha_{imp}$ and $\bar{\tau}_{ret} < 1\,\text{year}$. For example, for $T_{imp} = 7$ years, it is met that $\overline{R^2} \gtrsim 0.85$ and $\bar{T}_{ret} \approx T_{imp}$ when $SNR \gtrsim 0.004$, although $\bar{\alpha}_{ret} \approx 0.8\,\alpha_{imp}$ and $\bar{\tau}_{ret}$~320 days (Supplementary Fig. 9e-9h). (c) For imposed periods $T_{imp} \lesssim 6 - 7$ years, our filtering method cannot accurately retrieve long-term trends, independently of the signal-to-noise ratio (Supplementary Fig. 9i-9l). (d) When our filtering process is applied to a

synthetic signal without an imposed trend (or with very low signal-to-noise ratio), a spurious trend can be retrieved (Supplementary Fig. 4e-4f). In subsection 2.6, we present a methodology to discern between actual hidden long-term trends and spurious signals associated with high levels of noise.

4. We apply the efficient low-pass filtering technique (Technique 11 with $k = 10$ iterations) to the daily median brightness temperature difference ($\overline{\Delta T}_{M,K}(t)$) obtained for the seven target volcanoes. This yields the so-called median anomaly or $\overline{\delta T}$, which is then 1-year time-shifted to account for the delay produced by the filtering process (Supplementary Fig. 1h). Note that $\overline{\delta T} < 0$ (because $T_{c,M} < T_{h,K}$), has units of temperature, captures the long-term (~years) variations of median brightness temperature of the coldest parts of volcanoes with respect to the regional background, and its amplitude of variation must be considered a minimum estimate because part of it may be missed during the filtering process (see Methods and Supplementary Fig. 9g, 9k). It is also worth highlighting that $\overline{\delta T}$ is calculated using brightness temperature as measurement variable instead of real temperatures, whose calculation is more complex because it requires taking into account the pixel emissivity. However, the error that this produces in the calculation of pre-eruptive surface warming is negligible (Supplementary Methods; Supplementary Fig. 10).

2.6) Uncertainty analysis

Allocating uncertainties is crucial to assess the significance of the variations of the median anomaly time series ($\overline{\delta T}(t)$). The major source of uncertainty in $\overline{\delta T}(t)$, associated with the filtering process, is assessed through Monte Carlo experiments (shaded bands of Fig. 2a-2d):

1. We generate synthetic time series with a bootstrapping method (commonly used in seismic data processing[25]) consisting of resampling the daily median brightness temperature difference time series $\overline{\Delta T}_{M,K}(t)$. In particular, each element *j* of the synthetic time series is selected randomly from the elements *j*-1, *j*, *j*+1 of $\overline{\Delta T}_{M,K}(t)$ (the values of the first and last elements of the synthetic time series are chosen to be equal to the values of the second and penultimate values, respectively). This technique yields synthetic time series with the same mean and standard deviation as $\overline{\Delta T}_{M,K}(t)$.

2. We apply the best denoising technique designed in section 2.5 to the aforementioned synthetic time series. The result yields $\overline{\delta T}^{*}(t)$, which is then compared with $\overline{\delta T}(t)$ by calculating the difference between each data point of the time series.

3. We repeat 1,000 times the steps 1-to-2. This provides 1,000 values of the difference $\overline{\delta T}(t) - \overline{\delta T}^{*}(t)$ for each data point *j*, which is then used to determine the y-axis uncertainty of $\overline{\delta T}(t)$ at the 95% confidence interval (Supplementary Fig. 1g). Note that this approach also captures the uncertainty associated with the time lag produced by the filtering process.

4. For simplicity, we rescale $\overline{\delta T}$ (with its uncertainty), so it is always ≥ 0.

On the other hand, a spurious trend may appear in the filtered time series as consequence of the high levels of noise (see section 2.5 and Supplementary Fig. 4e-4f). The probability that the observed trends are spurious is assessed in terms of the maximum amplitude of variation of $\overline{\delta T}$ (Fig. 2f):

1. We design a synthetic time series composed of a zero-mean Gaussian noise with the same standard deviation as the daily median brightness temperature difference time series ($\overline{\Delta T}_{M,K}(t)$).

2. We apply the best denoising technique designed in section 2.5 to the aforementioned synthetic signal.

3. We repeat 10,000 times the steps 1-to-2. This is used to calculate the probability of obtaining by chance a spurious trend with the same amplitude or larger than the amplitude of the median anomaly time series $\overline{\delta T}$.

Data availability. Data (MODIS Terra/Aqua Calibrated Radiances 5-Min Level-1B Swath 1km V006 and MODIS Terra/Aqua Geolocation Fields 5-Min Level-1A Swath 1km V006) are available fully, openly, and without restrictions at https://earthdata.nasa.gov/.

Code availability. Two Matlab scripts for data processing and analysis are available (contact the corresponding author for further details).

REFERENCES

1. Chiodini, G. *et al.* Carbon dioxide diffuse degassing and estimation of heat release from volcanic and hydrothermal systems. *J. Geophys. Res. Solid Earth* **110**, B08204 (2005).

2. Lewicki, J. L., Connor, C., St-Amand, K., Stix, J. & Spinner, W. Self-potential, soil CO2 flux, and temperature on Masaya volcano, Nicaragua. *Geophys. Res. Lett.* **30**, 2–5 (2003).

3. Caliro, S. *et al.* Recent activity of Nisyros volcano (Greece) inferred from structural, geochemical and seismological data. *Bull. Volcanol.* **67**, 358–369 (2005).

4. Granieri, D., Avino, R. & Chiodini, G. Carbon dioxide diffuse emission from the soil: ten years of observations at Vesuvio and Campi Flegrei (Pozzuoli), and linkages with volcanic activity. *Bull. Volcanol.* **72**, 103–118 (2010).

5. Harris, A. J. L., Lodato, L. & Dehn, J. Thermal characterization of the Vulcano fumarole field. *Bull. Volcanol.* (2008). doi:10.1007/s00445-008-0236-8.

6. Chiodini, G. *et al.* CO2 degassing and energy release at Solfatara volcano, Campi Flegrei, Italy. *J. Geophys. Res. Solid Earth* **106**, 16213–16221 (2001).

7. Mannini, S., Harris, A. J. L. & Jessop, D. E. Combining Ground - and ASTER - Based Thermal Measurements to Constrain Fumarole Field Heat Budgets : The Case of Vulcano Fossa 2000 – 2019 Geophysical Research Letters. 1–10 (2019). doi:10.1029/2019GL084013

8. Ahmad, S. . P. *et al.* MODIS radiances and reflectances for earth system science studies and environmental applications. *Proc. 18th Int. Conf. Interact. Inf. Process. Syst. Meteorol. Oceanogr. Hydrol.* 188–192 (2002).

9. Brombach, T., Hunziker, C., Chiodini, G., Cardellini, C. & Marini, L. Soil diffuse degassing and thermal energy fluxes from the southern Lakki plain, Nisyros (Greece). *Geophys. Res. Lett.* **28**, 69–72 (2001).

10. Hernández, P. A. *et al.* Diffuse emission of CO2 from Miyakejima volcano, Japan. *Chem. Geol.* **177**, 175–185 (2001).

11. Frondini, F. *et al.* Diffuse CO2 degassing at Vesuvio, Italy. *Bull. Volcanol.* **66**, 642–651 (2004).

12. Perez, N. *et al.* Diffuse CO2 and 222Rn degassing from San Salvador volcano, El Salvador, Central America. 227–236 (2004).

13. Notsu, K. *et al.* Diffuse CO2 efflux from Iwojima volcano, Izu-Ogasawara arc, Japan. *J. Volcanol. Geotherm. Res.* **139**, 147–161 (2005).

14. Toutain, J.-P. *et al.* Structure and CO2 budget of Merapi volcano during inter-eruptive periods. *Bull. Volcanol.* **71**, 815–826 (2009).

15. Wright, R., Flynn, L. P., Garbeil, H., Harris, A. J. L. & Pilger, E. MODVOLC: near-real-time thermal monitoring of global volcanism. **135**, 29–49 (2004).

16. Coppola, D., Laiolo, M., Cigolini, C., Donne, D. D. & Ripepe, M. Enhanced volcanic hot-spot detection using MODIS IR data: results from the MIROVA system. *Geol. Soc. London, Spec. Publ.* **426**, 181–205 (2015).

17. Reath, K. A., Ramsey, M. S., Dehn, J. & Webley, P. W. Predicting eruptions from precursory activity using remote sensing data hybridization. *J. Volcanol. Geotherm. Res.* **321**, 18–30 (2016).

18. Manen, S. M. Van & Dehn, J. Satellite remote sensing of thermal activity at Bezymianny and Kliuchevskoi from 1993 to 1998. **37**, 983–986 (2009).

19. Lacava, T. *et al.* Thermal Monitoring of Eyjafjöll Volcano Eruptions by Means of Infrared MODIS Data. **7**, 3393–3401 (2014).

20. Laiolo, M. *et al.* Evidences of volcanic unrest on high-temperature fumaroles by satellite thermal monitoring: The case of Santa Ana volcano, El Salvador. *J. Volcanol. Geotherm. Res.* **340**, 170–179 (2017).

21. Marchese, F. *et al.* Inferring phases of thermal unrest at Mt . Asama (Japan) from infrared satellite observations. *J. Volcanol. Geotherm. Res.* **237**–**238**, 10–18 (2012).

22. Murase, M. *et al.* Preparatory process preceding the 2014 eruption of Mount Ontake volcano, Japan: insights from precise leveling measurements. *Earth, Planets Sp.* **68**, (2016).

23. Sano, Y., Kagoshima, T., Takahata, N., Nishio, Y. & Roulleau, E. Ten-year helium anomaly prior to the 2014 Mt Ontake eruption. *Sci. Rep.* **5**, 13069 (2015).

24. Kilgour, G. *et al.* The 25 September 2007 eruption of Mount Ruapehu, New Zealand: Directed ballistics, surtseyan jets, and ice-slurry lahars. *J. Volcanol. Geotherm. Res.* **191**, 1–14 (2010).

25. Caudron, C. *et al.* Change in seismic attenuation as a long-term precursor of gas-driven eruptions. *Geology* (2019). doi:10 .1130 /G46107.1.

26. Girona, T., Huber, C. & Caudron, C. Sensitivity to lunar cycles prior to the 2007 eruption of Ruapehu volcano. **8**, 1–9 (2018).

27. Chiodini, G. *et al.* The Domuyo volcanic system: An enormous geothermal resource in Argentine Patagonia. *J. Volcanol. Geotherm. Res.* **274**, 71–77 (2014).

28. D'Elia, L., Hernando, I., Páez, G., Petrinovic, I. & Vilarrosa, G. Erupciones y explosiones hidrotermales holocenas e históricas del Humazo, Campo Geotermal Domuyo: Dinámica y modelos eruptivos. in *VII Congreso Latinoamericano de Sedimentología y XV Reunión Argentina de Sedimentología* (2016).

29. Delgado, F., Pritchard, M. E., Ebmeier, S., González, P. & Lara, L. Recent unrest (2002–2015) imaged by space geodesy at the highest risk Chilean volcanoes: Villarrica, Llaima, and Calbuco (Southern Andes). *J. Volcanol. Geotherm. Res.* **344**, 270–288 (2017).

30. Morgado, E. *et al.* Old magma and a new, intrusive trigger: using diffusion chronometry to understand the rapid-onset Calbuco eruption, April 2015 (Southern Chile). *Contrib. Min.* (2019).

31. Bull, K. *et al.* The 2009 eruption of Redoubt volcano, Alaska. in (ed. Schaefer, J. R.) (State of Alaska, Department of Natural Resources, 2012).

32. Program, G. V. *Report on Agung (Indonesia)*. (Smithsonian Institution, 2018). doi:https://doi.org/10.5479/si.GVP.BGVN201801-264020

33. Global Volcanism Program. *Report on Agung (Indonesia)*. (Smithsonian Institution, 2003). doi:https://doi.org/10.5479/si.GVP.BGVN200303-264020

34. Dionis, S. M. *et al.* Diffuse CO2 degassing and volcanic activity at Cape Verde Islands, West Africa. *Earth, Planets Sp.* **67**, (2015).

35. Dionis, S. M. *et al.* Diffuse volcanic gas emission and thermal energy release from the

summit crater of Pico do Fogo, Cape Verde. *Bull. Volcanol.* **77**, (2015).

36. Program, G. V. *Report on Fogo (Cape Verde) — November 2014*. (Smithsonian Institution, 2014). doi:https://doi.org/10.5479/si.GVP.BGVN201411-384010

37. Curtis, A. & Kyle, P. Methods for mapping and monitoring global glaciovolcanism. *J. Volcanol. Geotherm. Res.* **333**–**334**, 134–144 (2017).

38. Allard, P. *et al.* Eruptive and diffuse emissions of CO<inf>2</inf> from Mount Etna. *Nature* **351**, 387–391 (1991).

39. Schwandner, F. M., Seward, T. M., Gize, A. P., Hall, P. A. & Dietrich, V. J. Diffuse emission of organic trace gases from the flank and crater of a quiescent active volcano (Vulcano, Aeolian Islands, Italy). *J. Geophys. Res. Atmos.* **109**, n/a-n/a (2004).

40. Kern, C., Masias, P., Apaza, F., Reath, K. A. & Platt, U. Remote measurement of high preeruptive water vapor emissions at Sabancaya volcano by passive differential optical absorption spectroscopy. *J. Geophys. Res. Solid Earth* **122**, 3540–3564 (2017).

41. Wenny, B. N., Xiong, X., Madhavan, S., Wu, A. & Li, Y. Long-term band-to-band calibration stability of MODIS thermal emissive bands. *Ocean Sens. Monit. V* **8724**, 872412 (2013).

42. Li, Z. L. *et al.* Satellite-derived land surface temperature: Current status and perspectives. *Remote Sens. Environ.* **131**, 14–37 (2013).

43. Billings, S. A. & Lee, K. L. A smoothing algorithm for nonlinear time series. *Int. J. Bifurc. Chaos* **14**, 1037–1051 (2004).

44. Guild, W. R. Note on heat transfer at the soil surface. *J. Meteorol.* **7**, 140–144 (1950).

45. Murphy, S. W., Oppenheimer, C. & de Souza Filho, C. R. Remote Sensing of Environment Calculating radiant fl ux from thermally mixed pixels using a spectral library. *Remote Sens. Environ.* **142**, 83–94 (2014).

Corresponding author. Correspondence and request for materials should be addressed to T. Girona. E-mail address: tarsilo.girona@gmail.com.

Acknowledgements. T. Girona is supported by an appointment to the NASA Postdoctoral Program at the Jet Propulsion Laboratory, California Institute of Technology, administered by Universities Space Research Association under contract with the National Aeronautics and Space Administration. Authors appreciate discussions on the matters of this paper with Á. Amigo and members of the Observatorio Volcanológico de Los Andes del Sur (OVDAS) - Servicio Nacional de Geología y Minería (Sernageomin); S. García and members of the Servicio Geológico Minero (SEGEMAR) and Comisión Nacional de Actividades Espaciales (CONAE).

Supplementary Information is linked to the online version of the paper at www.nature.com/nature.

Author Contributions. T.G. conceived the idea and led the data analysis and writing of the manuscript. V.R. and P.L. collaborated in writing the manuscript and designing figures. T.G., V.R., and P.L. discussed the new algorithm, model, results, and conclusions.

Author Information

- Reprints and permissions information is available at www.nature.com/reprints.
- The authors declare that they have no competing interests.
- Correspondence and requests for materials should be addressed to tarsilo.girona@jpl.nasa.gov.

FIGURES AND TABLES

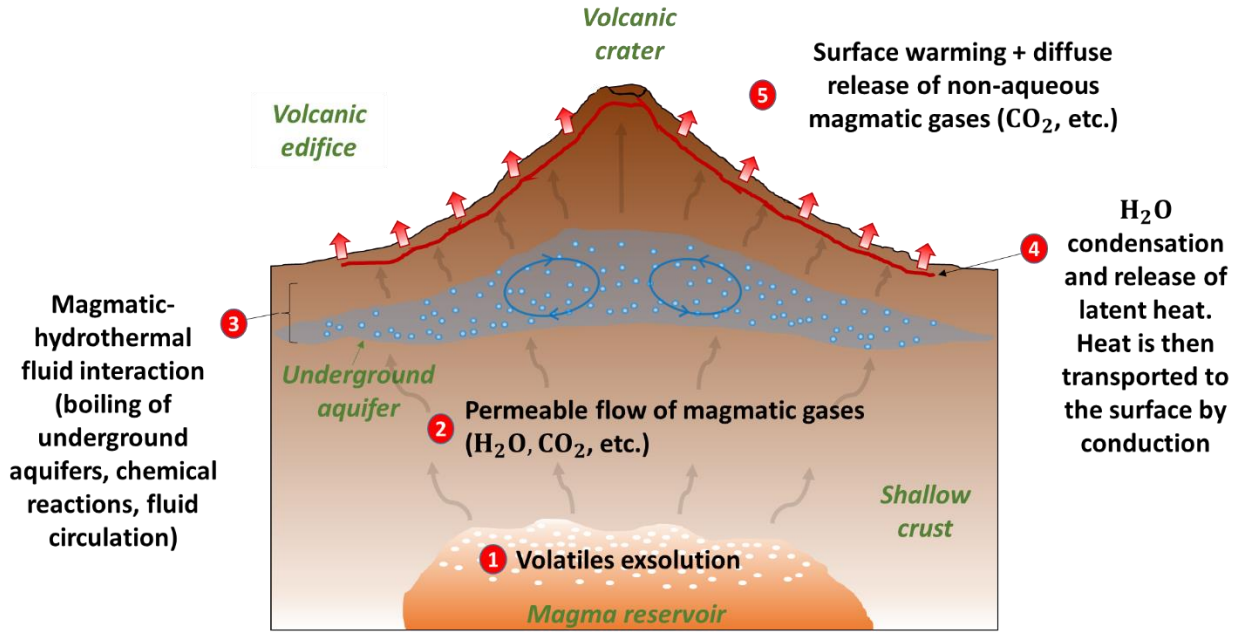

Figure 1. Fundamentals of large-scale (~volcanic edifice size) diffuse heating. Diffuse heating is the manifestation of underground magmatic-hydrothermal fluid interaction, and is controlled by the supply of hot magmatic gases from depth. In particular, magmatic gases escape from shallow reservoirs through the crust via permeable flow (grey arrows) and produce the boiling of underground aquifers (blue circles). Water vapor rising from the boiling aquifers (and from magma) condenses beneath the soil (red line), thus releasing latent heat that is transported via conduction to the surface[6,9] (red arrows). This heat increases soil temperature and radiance.

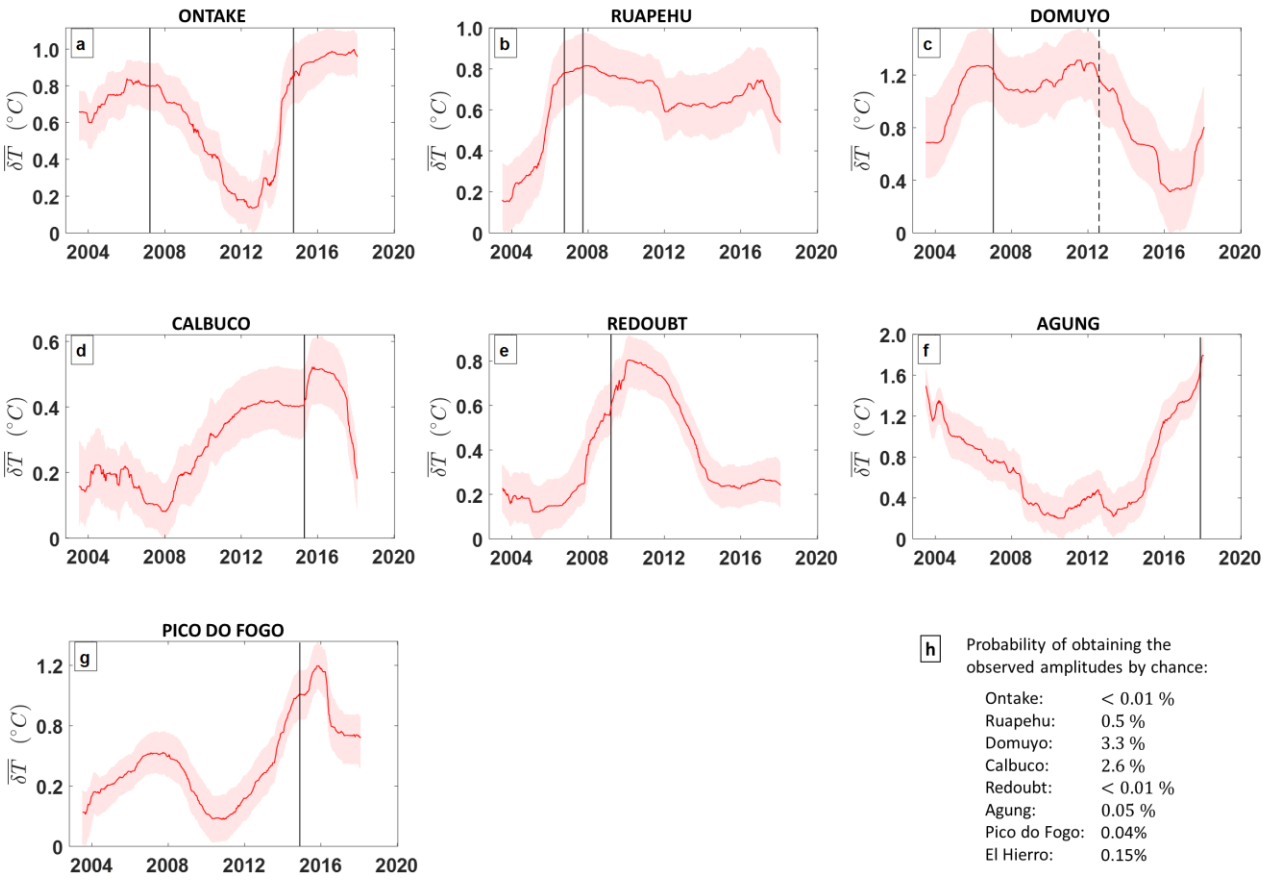

Figure 2. Diffuse heating time series obtained for the target volcanoes. **(a-g)** Results for Ontake, Ruapehu, Domuyo, Calbuco, Redoubt, Agung, and Pico do Fodo. The solid red line is the median anomaly $\overline{\delta T}$; the shaded bands represent its uncertainty (95% confidence interval); and the black vertical lines represent the onset of magmatic, phreatic, and hydrothermal eruptions. The dashed line of Domuyo (set at August 1, 2012) depicts a hydrothermal explosion that occurred during the 2012 austral winter, although the precise date is not well documented. **(h)** Probability of obtaining the observed amplitudes by chance.

Table 1. Changes of diffuse heat flux calculated from the median anomaly.

Volcano	Eruption start date	Type of eruption	$\overline{\delta T}(t) - \overline{\delta T}(t_0)$ (°C) [*1]	$\Delta\Phi_d(t; t_0)$ (W/m^2) [*2]
Ontake	2007 March 24 ($\pm$ 7 days)	Gas explosion (VEI=0)	$0.20\ (0.02 - 0.38)$	$0.88\ (0.05 - 1.71)$
	2014 September 27	Phreatic (VEI=3)	$0.72\ (0.51 - 0.93)$	$3.2\ (1.9 - 4.5)$
Ruapehu	2006 October 4 – 2007 September 25 [*3]	Gas explosion –phreatomagmatic (VEI=1)	$0.65\ (0.42 - 0.88)$ [*4]	$2.9\ (1.7 - 4.1)$ [*4]
Domuyo	2007 January 17	Hydrothermal explosion (VEI=0)	$0.55\ (0.15 - 0.95)$ [*4]	$2.5\ (0.5 - 4.5)$ [*4]
	2012 austral winter	Hydrothermal explosion (VEI=0)	$0.10\ (0 - 0.50)$	$0.4\ (0 - 2.1)$ [*5]
Calbuco	2015 April 22	Magmatic (VEI=4)	$0.32\ (0.19 - 0.45)$	$1.50\ (0.81 - 2.19)$
Redoubt	2009 March 15	Magmatic (VEI=3)	$0.47\ (0.30 - 0.64)$	$1.89\ (1.07 - 2.71)$
Agung	2017 November 21	Magmatic (VEI=3)	$1.42\ (1.15 - 1.69)$	$7.42\ (5.05 - 9.79)$
Pico do Fogo	2014 November 23	Magmatic (VEI=3)	$0.82\ (0.59 - 1.05)$	$4.38\ (3.01 - 5.75)$

[*1]Pre-eruptive warming, i.e., median anomaly difference between the onset of an eruption ($\overline{\delta T}(t)$) and the onset of the pre-eruptive warming phase ($\overline{\delta T}(t_0)$). [*2]Pre-eruptive increase of diffuse heat flux; this is calculated with equation (1) using: a realistic range for the time-averaged median surface emissivity ($\varepsilon = 0.95 \pm 0.05$) and the time-averaged median brightness temperature of the regional background (T) calculated from the radiance data (see Supplementary Table 1). Numbers in parentheses represent the 95% confidence interval, calculated from the uncertainty band in Fig. 2 and the general rule of error propagation. [*3]Our method does not allow us to distinguish different events occurring over such a short time. [*4]These are minimum estimates because the eruptions did occur at the beginning of the time series and thus part of the pre-eruptive increase may have been missed. [*5]This is calculated by setting the 2012 hydrothermal explosion at August 1, 2012 (Fig. 2c); the explosion occurred during the 2012 austral winter, although the precise date is not well documented.